國立臺灣大學理學院物理研究所
碩士論文
Graduate Institute of Physics
College of Science
National Taiwan University
Master Thesis

原恆星盤 MWC 758 裡的塵埃懸臂
Spirals in the circumstellar disk - MWC 758

沈柏廷
Bo-Ting Shen

指導教授：李景輝 博士
湯雅雯 博士
高培邁 博士
Advisor: Chin-Fei Lee, Ph.D.
Ya-Wen Tang, Ph.D.
Patrick Koch, Ph.D.

中華民國 108 年 1 月
January, 2019

doi:10.6342/NTU201900272

國立臺灣大學碩士學位論文
口試委員會審定書

原恆星盤 MWC 758 裡的塵埃懸臂
Spirals in the circumstellar disk – MWC 758

本論文係沈柏廷君（學號 R06222012）在國立臺灣大學物理學系、所完成之碩士學位論文，於民國 108 年 01 月 18 日承下列考試委員審查通過及口試及格，特此證明

口試委員：

（簽名）

（指導教授）

doi:10.6342/NTU201900272

誌謝

超級大感謝我的老闆湯湯 & 大老闆 Patrick。萬幸自己遇到了超棒的老闆們。

感謝老闆湯湯用心認真好相處給我大大大大大大大幫助。讓我從不認識天文到做出一點研究成果。從處理數據作圖到寫程式分析並討論研究成果，教我的不只是學術，更是學習，學習解決問題的能力。

感謝大老闆 Patrick 給我薪水，補助出國觀測與參加年會的費用，並傾心協助我完成論文。感謝大老闆給我機會去夏威夷觀測三次。

感謝女朋友佳鴻的陪伴關心與幫助鼓勵，讓我不再迷惘停留，使我認真向上前進，開心做事並完成進度。謝謝你讓我成為一個更好的人，謝謝：)

感謝 Group 的佩穎 & 士韋，被我纏著問問題 xD

感謝小弟宜珊 & Teresa，一起認真學習討論準備咕嚕咪挺。

感謝侯冠州學長的幫助，人在以色列還要被我用小視窗問各種問題:P

感謝天文社 x IAA，吳俊儒 王瑋晨 陳立馨 黃于瑄 鄧郁璇 何適楷

感謝麒瑞凱風，是你們帶我走入天文的坑 xD 如果不是和你們一起，我也不會有勇氣在 Paul's Meeting 後去找湯湯，爾後一路走到這。

祝福所有在天文路上的夥伴們都一路順利：)

感謝雪峰教授從大一開始的導生互動^_

感謝我的口試委員們。

感謝可愛的蛋蛋；感謝被我放閃的日文系 Mizu ；感謝一起做天文的暑期學生們；謝謝大家：)

最後，我想要特別感謝爸爸媽媽。感謝你們給了我聰穎的腦袋，而我也會更認真努力學習。感謝你們全心的支持與鼓勵，讓我能夠無後顧之憂，大步向前邁進。謝謝：)

doi:10.6342/NTU201900272

中文摘要

行星是在原恆星盤面裡面形成，並在盤面產生非對稱性的構造。我們可以使用高解析力和高靈敏度的阿塔卡瑪大型毫米及次毫米波陣列干涉儀 (ALMA) 來觀測原恆星盤系統並研究行星形成。盤面的非對稱性結構能夠提供間接的證據來找尋隱藏在盤面裡的物體。

我們使用 0.9 毫米的波段來分析原恆星盤 MWC 758 的塵埃分佈。我們將盤面每隔 5 度分割成 72 個小扇形來分析結構。對於每一個扇形，我們畫出強度對半徑的分佈圖，並使用兩個高斯函數來描述這個散佈圖。

我們使用得到的高斯參數來代表盤面上的峰值位置。我們把高斯的強度與位置與對角度作圖來做進一步分析得到細部構造。我們找到了 3 個非對稱性的特徵結構。這三個結構中，有兩個是塵埃團，它們在不同的半徑但都帶有懸臂構造的尾巴。第三個是一個懸臂的構造在盤面的東南方。

我們使用懸臂密度波理論來分析我們看到的懸臂特徵。隱藏在盤面裡的天體能夠透過重力擾動盤面而形成懸臂的特徵。根據數學模型推導的解析解可以得出理論的懸臂形狀。我們使用上述的方程式來分析觀測到的三個懸臂。觀測到的三個特徵可以用被行星引起的懸臂密度波理論解釋，並推測三個行星的可能位置。

我們比較在毫米波段看到的懸臂與紅外線偏振光觀測到的懸臂位置。紅外線的懸臂座落在毫米懸臂的內側，這樣的結構可以用散射來解釋。紅外線所觀測到的是打在毫米懸臂結構上的散射光。此外，兩波段的懸臂距離在西北方 (近) 較大而東南方 (遠) 較小，這樣的現象可以用傾斜盤面的遠近來解釋。

我們比較我們觀測的結果並與更高解析度的新圖片比較，我們得出不一樣的結構運用不一樣的分析方法，而我們觀測到的結構也出現在高解析度的新圖片裡。

關鍵字：原恆星盤、恆星 (MWC 758)、行星與盤的互動、塵埃懸臂

doi:10.6342/NTU201900272

Abstract

Planets formed within disks such as the Solar System and expected to induced substructures within disks. With Atacama Large Millimeter/submillimeter Array (ALMA), we can probe into protoplanetary systems to study planets formation. Asymmetrical features within disks might provide the indirect evidences of embedded objects. We analyze the disk structures of MWC 758 traced with the continuum emission at wavelengths of 0.9 millimeter (mm). We split the dust ring into segments in azimuth to study the disk structure. For each segment, we fit two Gaussian functions to the intensity versus radius profile. We analyze the best-fit parameters as a function of azimuth. We describe the disk geometry with peak locations. We find asymmetries and identify three structures. Among the three, two (arm 2 and arm 3) are dust clumps at different radius with similar intensity profiles and a spiral-like tail. The third feature (arm 1) is a spiral-like structure located at southeast. We compare our spirals with the spirals seen in the near-infrared (NIR) polarized intensity. The counterparts of arm 1 and arm 2 in the NIR appear at smaller radius than our spirals. By comparing the spirals seen in the 0.9 mm and NIR, we found that the spatial offset can be explained by the scattering from the inner edge of the sub-mm spirals. Comparing the spirals in the sub-mm and in the NIR, there is a larger offset in arm 2 (near side) than in arm 1 (far side) due to the projection effect of the actual disk geometry. We fit our features with the spiral density wave theory using the WKB approximation and results in two sets of disk aspect ratio. One is relatively

doi:10.6342/NTU201900272

low value (∼0.03), and the other is the upper bound of the parameter (∼0.2). The planet locations predicted by the upper bounded result are similar to the one determined by Benisty et al. (2015). The spiral patterns can be explained by the density wave induced by the planets. We compare our spirals with a higher-resolution ALMA image by Dong et al. (2018). We identify different structures in the West of the disk due to the resolution of the image and the analysis method.

Key words: protoplanetary disks — stars: individual (MWC 758) — planet-disk interactions — spirals

doi:10.6342/NTU201900272

Contents

doi:10.6342/NTU201900272

doi:10.6342/NTU201900272

doi:10.6342/NTU201900272

List of Figures

doi:10.6342/NTU201900272

List of Tables

doi:10.6342/NTU201900272

Chapter 1

Introduction

The origin and the evolution history of our Solar system is one of our biggest interests. Although we have observed and confirmed ∼3000 exoplanets in the debris disks (http://exoplanets.org/), when and where the planets start to form still remains as an open question. A planet is closely related to the search of the alien and possible habitat for future human. Different from stars, a planet is not able to generate lights for us to directly detect. Instead, we can search the indirect evidences induced by the embedded objects.

Embedded planets can perturb disks through gravitational interaction and produce asymmetrical structures such as vortices, spirals and gaps (Zhu & Stone, 2014). Such observed structures can constrain the physical quantities of the embedded planets, such as the mass and the location. A spiral feature can be explained by the density wave excited by an embedded object (Lin & Shu, 1964; Ogilvie & Lubow, 2002). This method was used in the disks of SAO 206462 (Muto et al., 2012), V1247 Orionis (Kraus et al., 2017) and MWC 758 (Benisty et al., 2015) to explain the spiral features. Gaps in disks can be opened by planets. With the gap locations and widths, we can estimate the mass of the planets (Kanagawa et al., 2015). A planet embedded in a disk can produce a dust trapping vortex at the edge of an eccentric gas gap with a three-dimension magnetohydrodynamic simulation considering the ambipolar diffusion (Zhu & Stone, 2014). The asymmetrical structures in the early stage disks are the keys to answer when the planets formed.

We need good telescopes to probe the compact structures in protoplanetary systems. Improving from single-dish telescopes to interferometries, such as the Submillimeter Ar-

doi:10.6342/NTU201900272

ray (SMA) and the Atacama Large Millimeter Array (ALMA), we can reach unprecedented sensitivities and resolutions. ALMA have multiple bands in millimeter (mm) and sub-millimeter (sub-mm) wavelengths. The spectral energy at this wavelengths is mostly from the thermal radiation of dust grains with sub-mm in size. The mm emission has lower optical depth which provides the information from the colder disk midplane, where the dust grains are located. The typical temperatures of disk mid plane are >100K in 10 au and 10K at 100 au in radius (Dutrey et al., 2014). With ALMA, the high resolution image at sub-mm wavelengths, we can study the detail structures of the circumstellar disks for planet formations.

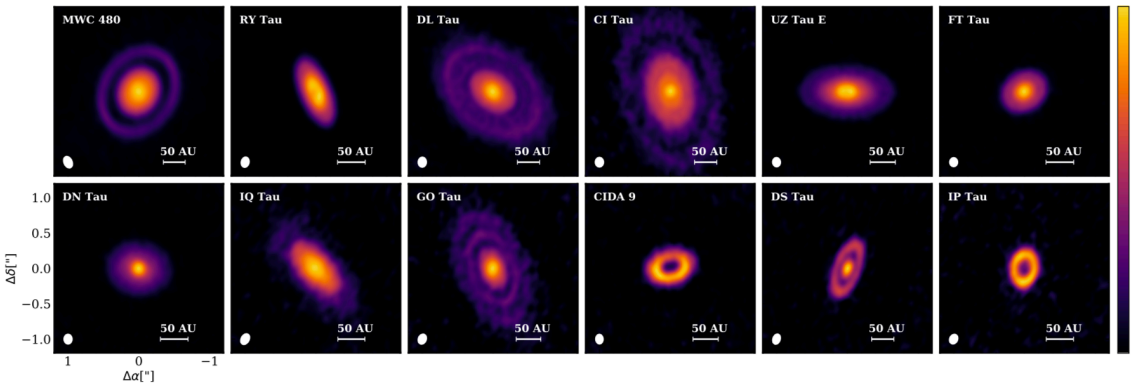

Figure 1.1: Rings and gaps of protoplanetary disks observed by ALMA with ∼0.″12 resolution at band 6 (1.3 mm wavelengths). The rings and gaps could all be well explained by low-mass planets with low viscosity disks. This image is from Long et al. (2018) Fig. 1.

Several asymmetric features have been found in circumstellar disks by ALMA. For example, Long et al. (2018) reports half of the survey of 32 disks in the Taurus molecular cloud in band 6 (wavelengths of 1.33 mm, 226 GHz) with an angular resolution of 0.″12, and the results are shown in figure 1.1. The rings and gaps could all be well explained by low-mass planets with low viscosity disks. Another example is the V1247 Orionis system, where an asymmetric ring and a crescent structure was detected with 0.″04 resolution in band 7 (wavelengths of 870 μm) continuum with ALMA (Kraus et al., 2017). In this system, it is suggested that a planet at 100 au produce the gap and trigger two vortices, the crescent and the asymmetry in the ring, based on the hydrodynamics simulations (Kraus et al., 2017). Around HD135344B, a ring and an arc was detected in ALMA band 7

doi:10.6342/NTU201900272

(wavelengths of 890 μm) with 0.″16 resolution using superuniform (van der Marel et al., 2016). Two planets at different locations were a possible scenario to form the vortices and the scattered light image. A spiral feature was also seen in the CO emission of HD 142527 by ALMA (Christiaens et al., 2014). The asymmetrical structures provide the indirect evidences for the embedded objects.

List of objects were observed by ALMA, we targeted a special candidate MWC 758 to study the planet formations. MWC 758 is a Herbig A5 star (Thi et al., 2001).The distance is 151^{+9}_{-8} parsec (Holl et al., 2018) (See appendix E). Its age is 3.5$\pm$2 Myr, which is a relatively young star (Meeus et al., 2012). The inclination of the disk is 21°$\pm$2°, and the position angle of the major axis is 65°$\pm$7° east from north (Isella et al., 2010). The center star is estimated to be 2$\pm$0.2 $M_{\odot}$, which is an intermediate level star. An asymmetrical emission located at northwest $\sim$70 AU was detected in the sub-millimeter observation after subtracting a symmetrical model (Isella et al., 2010). MWC 758 has two spiral features in NIR scattered light image (Grady et al., 2013; Benisty et al., 2015). There is no bright arc emission in the NIR image to distinguish the near far side. The north disk is the near-side based on the trailing sense of the spirals seen in NIR (Grady et al., 2013). The disk mass is estimated to be 0.01 solar mass (Andrews et al., 2011).

A double-ring structure with two dust clumps is resolved in the ALMA band 7 sub-mm continuum observation with $\sim$0.″1 angular resolution. A spiral structure was seen in the ^{13}CO J=3-2 peak intensity image (Boehler et al., 2018). Reggiani et al. (2018) discovered a point-like structure and a third spiral at L' band (3.8μm) vecter vortex coronagraph at the Keck II telescope. Dong et al. (2018) presented ALMA cycle 5 band 7 continuum emission with $\sim$0.″04 angular resolution. The $\sim$mm dust ring has an eccentric cavity, triple rings, two-armed spirals and double clumps.

doi:10.6342/NTU201900272

Table 1.1: Main parameters of MWC 758

Parameter	Value	Reference
R.A.	05:30:27.53	(1)
Dec.	+25:19:56.67	(1)
Distance	151 pc	(2)
Age	3.5±2 Myr	(3)
Stellar mass	2±0.2 $M_{\odot}$	(4)
Disk inclination	21°±2°	(4)
Disk P.A.	65°±7°	(4)
Disk mass	0.01 $M_{\odot}$	(5)

NOTE–Reference: (1) SIMBAD, (2) GAIA, (3) Meeus et al. (2012), (4) Isella et al. (2010), (5) Andrews et al. (2011).

doi:10.6342/NTU201900272

Chapter 2

Observations and Imagings

We are re-processing the archival data to get a better image. The observations were carried out with ALMA in Cycle 2, Band 7 (project ” 2012.1.00725.S”) on Sep. 1 and Sep. 24, 2015, with an on-source integration time 29 and 24 mins, respectively. The calibration was done using pipeline. After standard calibrations, we applied self-calibration to the measurement set to get better images. The phase center of MWC 758 is at (α, δ)= (05:30:27.53, +25.19.56.67)

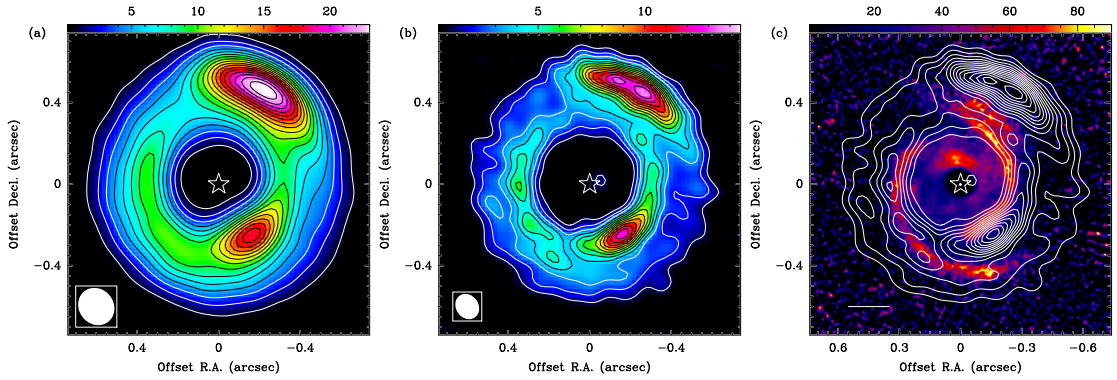

Figure 2.1: (a): The continuum emission at 330 GHz (0.9 mm) with robust weighting. The S/N of peak intensity is ∼134. The resolution (beam) is 0.″19×0.″17. Contours are -5, 5, 13, 21, 28, ..., 133 σ, where 1 σ is 92 μJy beam^{-1}. (b): The continuum emission with SU weighting. The S/N of peak intensity is ∼40. The resolution is 0.″13×0.″11. Contours are -3, 3, 6, 9, 12, ..., 39 σ, where 1 σ is 0.40 mJy beam^{-1}. (c): Polarized intensity image from NIR (Benisty et al., 2015) in color scale with continuum emission (contours) from panel b superimposed. The white segment denotes a scale bar of 30 au. In panel a and b, the corresponding angular resolution is shown as an ellipse at the lower-left corner and the lowest three contours are in white. The wedges in panel a and b are in mJy beam^{-1}. In all panels, the stellar location is marked as a star.

doi:10.6342/NTU201900272

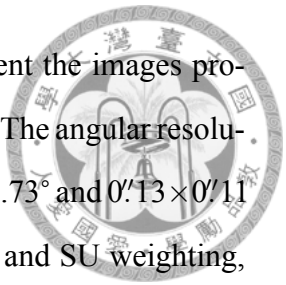

The continuum emission is well detected and resolved. We present the images produced with both robust weighting and super-uniform[1] (SU) weighting. The angular resolution of the continuum images are $0\farcs19\times0\farcs17$ with a position angle of 37.73° and $0\farcs13\times0\farcs11$ with a position angle of 35.02° for the images with robust weighting and SU weighting, respectively. The sensitivities (noise level) are 92 μJy beam^{-1} and 0.4 mJy beam^{-1} for the images with robust and SU weighting, respectively.

The image with robust weighting is shown in Fig. 2.1a. The total flux is 17.3 Jy beam^{-1}. The brightest emission is 23.8 mJy beam^{-1} (18.8 K) with a S/N $\sim$259, located at northwest with a banana-shaped structure. The second brightest emission is 18.1 mJy beam^{-1} (15.8 K) with a S/N $\sim$197, located at southwest linked with an arc from west to east. Between the banana-shaped structure and the arc are two fainter regions.

The image with SU weighting is shown in Fig. 2.1b. The total flux is 8.0 Jy beam^{-1}. The brightest emission is 13.6 mJy beam^{-1} (21.5 K) with a S/N $\sim$34, located at northwest with a more stretched banana-shaped structure extended $\sim90^\circ$. The second brightest emission is 12.6 mJy beam^{-1} (20.4 K) with a S/N $\sim$32, located at southwest with an arc extended $\sim180^\circ$ from south to north counterclockwise. The intensity minimum located at south (150°) separates a new arc at southeast.

Comparing robust and SU weighting, SU weighting decreases the flux density but has a better resolution. SU weighting reveals the structure at southeast and strengthen the variation between the banana-shaped structure and the southwest arc with a clear separation.

Table 2.1: Comparison of robust and SU weighting

	Robust	SU
Resolution	$0\farcs19\times0\farcs17$	$0\farcs13\times0\farcs11$
Total flux	17.3 Jy beam^{-1}	8.0 Jy beam^{-1}
Noise	92 μJy beam^{-1}	0.40 mJy beam^{-1}

[1]Super-uniform weighting is similar to uniform weighting with an additional sub-parameter 'npixels'. Npixels changes the number of uv-cell on a side to redefine the uv-plane. Neighboring cells share their weights which counts visibilities in a larger area. We adopt npixels = 4 which optimizes the flux density among npixels = 2, 4, 6.

doi:10.6342/NTU201900272

Chapter 3

Analysis

3.1 Inclined dust disk geometry

The inclined dust emissions exhibit high variations along both radial and azimuthal directions. We further analyze the dust emission traced with robust weighting in order to identify the large-scale disk geometry. The angular resolution is $\sim 0''.18$ with robust weighting, which is 25° in azimuth at a radius of $0''.4$. We compare the result with the projection effect.

We split the continuum emission every 10° in azimuth into 36 segments to have a sufficient sampling rate. The result is robust and consistent within error bar of different numbers of the segments. We analyze the intensity versus radius profile of each segment. We fit one Gaussian function to every segment to describe the profile. We use the amplitude and the position from a Gaussian fitting to represent the intensity and the peak location of the segment. Appendix A shows the result of the fittings.

Peak locations obtained from our analysis are not a circular ring. We fit an ellipse to the peak locations in order to describe the inclined dust disk geometry. The fitted ellipse center is shifted $(0''.0021 \pm 0''.0011, 0''.0707 \pm 0''.001)$ in RA and Dec relative to the phase center. Fig. 3.1 shows the result. With the best-fit ellipse, we calculate the inclination and the P.A. assuming the dust disk is a circular ring. Based on the dust peaks, the inclination is 36.0 ± 0.43° and the P.A. is 150.5 ± 0.78°. The details of the ellipsoidal fit and the error bars are shown in appendix F & G.

doi:10.6342/NTU201900272

The inclination angle and the major axis derived from the gas kinematics are 21° and 65°, respectively (Isella et al., 2010). The inclination and the P.A. calculated from the inclined dust ellipse clearly deviates from the known gas disk geometry. Together with the significant offset of the ellipse center, the continuum emission traced here is not tracing a circular structure by a projection effect.

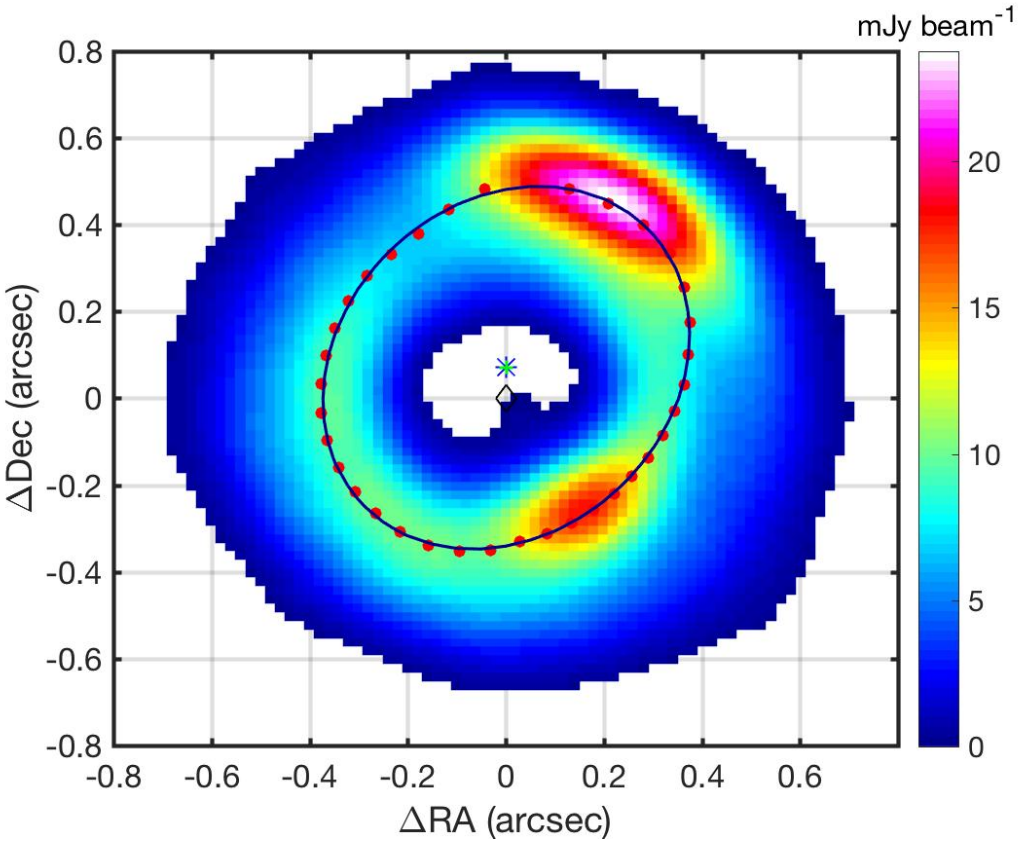

Figure 3.1: (a): Ellipsoidal fit to inclined dust emissions with robust weighting. The center of the fitted ellipse (marked with a blue star) is shifted north from the stellar location (marked with a diamond) by 0.″071±0.″001. The red circles are the peak locations obtained from the best-fit Gaussian of each segment. The black curve is the best-fit ellipse of the red circles.

3.2 Deprojection

The image we observed is a projection of the disk on the sky by its inclination. We do the deprojection in the image domain to recover the real disk geometry. The major axis is 65° and the inclination is 21° base on the ^{12}CO emission from Isella et al. (2010). First,

doi:10.6342/NTU201900272

We rotate the image with 25° counterclockwise to set the major axis lies on the horizontal axis. Second, expand the minor axis (the vertical axis) with one over cosine inclination ($\cos 21°$). Third, rotates 25° clockwise to set the major axis to it origins. We use the deprojected image for further analysis.

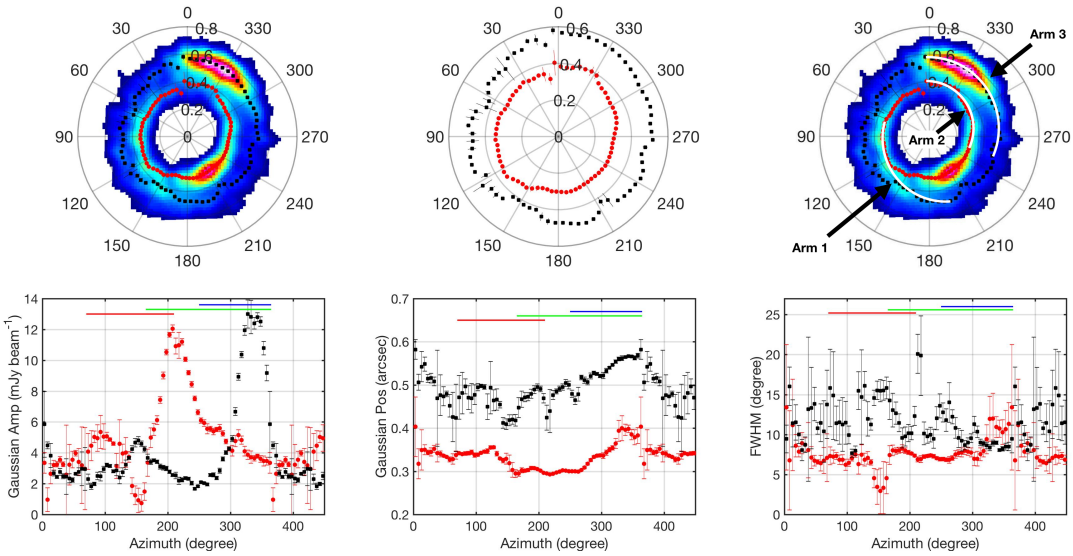

Figure 3.2: In all panels, the peak locations are obtained by two Gaussian fitting of each segment. Inner peak locations are marked with red circles and outer peak locations are marked with black squares (error bar of 95% confident level). (a): The deprojected image (color scale) with peak locations. (b): Peak locations in polar coordinates. (c): Three features superimposed with Fig. 3.2a. Bottom panels are the Gaussian function three parameters as a function of azimuth. Amplitude (left panel), position (middle panel) and FWHM (right panel).

3.3 Three features

After deprojecting with the major axis at 62° and the inclination at 21° based on the CO emission from Isella et al. (2010); Boehler et al. (2018), we use the same method in Sec. 3.1 to analyze the continuum emission with SU weighting. We will identify three features (arm 1, 2, 3) of the continuum emission from our analysis.

With the higher resolution image, we split the continuum emission into 72 segments. Every segment is 5° in azimuth. One synthesized beam is ∼3.4 data points in azimuth at 0.4 arcsec.

Instead of one Gaussian function, the profile of the deproected SU weighting image

doi:10.6342/NTU201900272

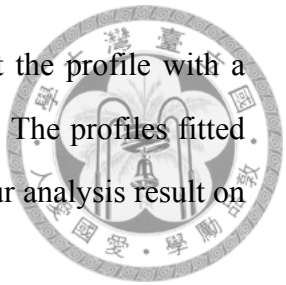

is better described by two Gaussian functions. (We also tried to fit the profile with a Gaussian-Hermite function, which will be discussed in appendix H.) The profiles fitted with two Gaussian functions are shown in appendix B. We overlay our analysis result on the continuum image in Fig. 3.2a.

Most segments are well described by the two Gaussians. Around the north clump (at azimuth $\sim 300°$), there are two components in the profiles but without a clear intensity minimum and a clear separation in radius between the two peaks. The profile is like a Gaussian function with a flat tail at an inner radius. This will result in a larger error bar of the inner Gaussian's position, because the second peak can not be well positioned by the flat tail. Fig. 3.2c. shows the results of Gaussian parameters with 95% confident level in error bars. We use the amplitudes and the positions of the two Gaussians to represent the peak locations and intensities in each segment. As a result, we see a trend in the position panel. The peak locations move in radius as a function of azimuth.

Three features are drawn with white lines in Fig. 3.2c. We now describe how we identify and localize relevant structural features in the above described figures. They are selected between intensity minimums and the position separations with the nearby peak locations. There are three brighter components with above 10 sigma (1 sigma is 0.4 mJy beam^{-1}) emission in the amplitude panel. The first component (north clump) is the brightest emission at northwest on the outer Gaussian (at azimuth $\sim 330°$). The second component (south clump) is the second brightest emission at southwest on the inner Gaussian (at azimuth $\sim 220°$). The third component is at southeast (at azimuth $\sim 140°$) with both inner and outer Gaussian's intensity greater than 10 sigma. Also comparing with the position panel, the inner Gaussian is moving outward until 130° in azimuth. The outer Gaussian is also moving outward starting from 140°. They show a similar moving trend, so they are connected from 130° (inner) to 140° (outer). We compare the position and the width with its neighbors to identify the start and end points of the features.

First, the brightest emission is a banana-shaped structure located at northwest (arm 3) from 365° to 250° in azimuth at a larger radius. The start point is at 365° at north instead of 370°. It intensity is just above ten sigma but the position and width is much deviates

doi:10.6342/NTU201900272

from the general trend. The end point is at 250°, which is the local minimum in intensity and the inner most region. The peak locations move inward from 0.″58 to 0.″46 in 115° with the pitch angle of ∼7.4°. (See appendix I for the definition of the pitch angle.)

Second, southwest arc is located from 250° to 365° in azimuth at an inner radius without the south clump. (South clump is located at the same radius.) The start point is 250° at West because this is the end point of the symmetry south clump intensity profile. The end point is at 365° which is explained above. The peak locations move outward from 0.″3 to 0.″4 in $\sim 150°$ with the pitch angle of ∼9.4°.

Third (arm 1), the southeast arc follows with the brighter emission from azimuth 70° to 130° for inner Gaussian and connects to the outer Gaussian from 140° to 210° in azimuth. The start point is at 70°, the intensities after are continuously above ten sigma in the intensity. Following with the brighter emission and comparing with the position panel, the third feature moves from the inner Gaussian (at 130°) to the outer Gaussian (at 140°). The end points is the local minimum at 210 °, which the next few points are much deviates from the general trend. The peak locations move outward from 0.″34 to 0.″49 in $\sim 140°$ with the pitch angle of ∼10.2°.

3.4 Toomre Q parameter

To calculate the gravitational stability, we introduce the Toomre Q parameter. (Toomre. 1964)

$$Q = \frac{c_s \Omega}{\pi G \Sigma} \tag{3.1}$$

Q is the Toomre Q parameter, where c_s is the sound speed obtained with the kinetic theory of gases, Ω is the orbital frequency, G is the gravitational constant, Σ is the disk surface density. (Sound speed in the disks is discussed in appendix J.)

For the brightest and second brightest emission in SU weighting, the brightness temperature is 21.5K and 20.4K, respectively. The temperature is 34K and 78K, respectively, from Boehler et al. (2018). With radiative transfer, we can calculate optical depth with 0.54

doi:10.6342/NTU201900272

and 0.19, respectively. With the dust opacity 2.74 cm^2 g^{-1} (Ossenkopf & Henning, 1994), we then calculate the surface density is 0.198 g cm^{-2} and 0.070 g cm^{-2}, respectively. The sound speed is $\sim$0.5km and the orbital frequency is $\sim 10^{-11}$ in unit s^{-1}. Finally, we get Toomre Q parameter for the two brightest emissions are 240 and 2704 ,respectively. The Q parameter here only considered the dust. Assuming gas-to-dust ratio to be 100, the Q parameter will be much lower to $\sim$2-27.

The gas-to-dust ratio in protoplanetary system still remains an open question. For similar system HD142525, the gas-to-dust ratio of peak emission are $\sim$3 for north clump and $\sim$30 for south clump and overall $\sim$10 to $\sim$30 (Muto et al., 2015). The gas-to-dust ratio in MWC 758 by Boehler et al. (2018) is $\sim$10 for the brightest emission. With the advised gas-to-dust ratio, Q will be larger than 1, which is gravitational stable.

3.5 Line widths

To calculate the turbulence level of the clumps, I fit one Gaussian function to the spectra of ^{13}CO emission (without continuum subtraction) at the peak pixels. (See appendix K for the line data and results). The width of the Gaussian function at the southwest and northwest peaks are 555.9 and 329.7 in m s^{-1}, respectively. The sound speeds are 478.2 and 315.9 in m s^{-1}, respectively. There is no clear turbulence level at the peaks.

3.6 Spiral feature modeling

From our analysis, the peak locations move in radius as a function of azimuth. We introduce a spiral model to explain the features. This method was used in the disks of SAO 206462 (Muto et al., 2012), V1247 Orionis (Kraus et al., 2017) and MWC 758 (Benisty et al., 2015) to explain the spiral features.

The model is based on the spiral density wave theory, where the planet embedded in the disk is known to launch spiral waves (Lin & Shu, 1964; Ogilvie & Lubow, 2002). The model was first predicted by Rafikov (2002), using WKB approximation.The spiral pattern can be described by the equation.

doi:10.6342/NTU201900272

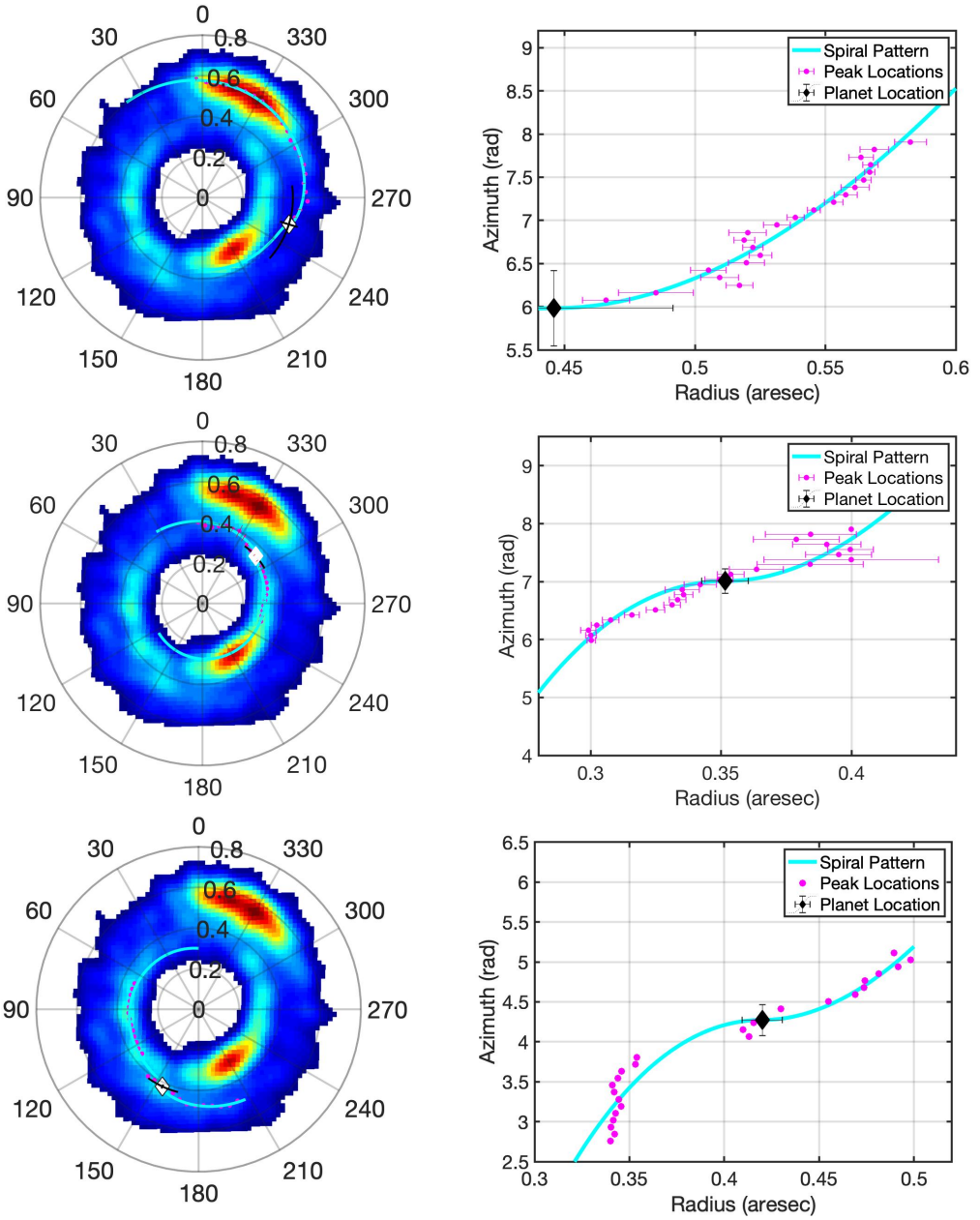

Figure 3.3: Results of NW(upper panel), SW(middle panel) and SE(bottom panel) spiral fitting. For left panels, color scale is the deprojected continuum emission with SU weighting. The red circles and the black squares are the peak locations. The blue line is the density wave launched by the predicted planet with 95% confident level in magenta arcs. The diamonds are the predicted planet location at (r_c, θ) = ($0''.45 \pm 0''.05$, $253.1° \pm 24.6°$), ($0''.35 \pm 0''.01$, $312° \pm 12°$) and ($0''.42 \pm 0''.01$, $154.7° \pm 11.5°$) for NW, SW and SE respectively. The disk aspect ratio (h_c) of three features are 0.03±0.02 for NW, 0.018±0.003 for SW and 0.027±0.003 for SE. For right panels, the axes are distance and azimuth. The red circles are the selected peak locations to fit with the spiral feature model. The blue curve is the best-fit result of the spiral feature. The diamond is the predicted planet locations.

doi:10.6342/NTU201900272

$$\theta(r) = \theta_0 + \frac{sgn(r - r_c)}{h_c}(\frac{r}{r_c})^{1+\beta}[\frac{1}{1+\beta} - \frac{1}{1-\alpha+\beta}(\frac{r}{r_c})^{-\alpha}] - \frac{sgn(r - r_c)}{h_c}(\frac{1}{1+\beta} - \frac{1}{1-\alpha+\beta}) \quad (3.2)$$

This equation has five parameters. The r_c and θ_0 is the launching point, the predicted planet location in polar coordinates. α is related to the disk's rotation, $\Omega(r) \propto r^{-\alpha}$. β is related to the sound speed (i.e., temperature), $c(r) \propto r^{-\beta}$. h_c is the disk aspect ratio. Disk aspect ratio is the ratio of the scale height to the radius at the location r_c, $h_c = c(r_c) / r_c \times \Omega(r_c)$ (Muto et al., 2012; Benisty et al., 2015). We fix α=1.5 assuming the disk is in Keplerian rotation and β=0.45 following Andrews et al. (2011).

We fit three features with the model. Fig. 3.3 shows the result of NW(upper panel), SW(middle panel) and SE(bottom panel) fitted with the spiral feature model. Diamonds are the predicted planet location at (r_c, θ_0) = ($0''.45 \pm 0''.05$, $253.1° \pm 24.6°$), ($0''.35 \pm 0''.01$, $312° \pm 12°$) and ($0''.42 \pm 0''.01$, $154.7° \pm 11.5°$) for NW, SW and SE, respectively. The disk aspect ratio (h_c) of three features are 0.03±0.02 for NW, 0.018±0.003 for SW and 0.027±0.003 for SE.

doi:10.6342/NTU201900272

Chapter 4

Discussion

4.1 Spirals

In order to check the degeneracy of the spiral model, I test my fitting with different bound values. With a smaller disk aspect ratio, the planet location tends to be closer to the spiral, while the pitch angle is larger around the planet. With setting a lower bound of h_c = 0, the spiral fittings result in small disk aspect ratios $\sim$0.03 of our features, with planets close to the spirals.

The disk aspect ratio of a rotationally flatted disk is typically $\sim$0.1. The disk aspect ratio is found to range from 0.05-0.25 obtained by a model which resolved the disks using scatter light data (Andrews, 2015). A low value indicates a colder disk, which is difficult to launch a spiral. The typical lower limit is h_c $\sim$0.01-0.03 (Muto et al., 2012). Our fitting results have small values of h_c which approach the lower limit to detect spirals in the colder disk.

The disk aspect ratio is the ratio of the scale height to the radius. The scale height is the ratio of the sound speed to the Keplarian angular speed. We calculate the disk aspect ratio by the definition directly. The sound speed is obtained by the kinetic theory of gases with the temperature profile from Boehler et al. (2018). With the central star of 2 solar mass, we can calculate the Keplarian angular speed. The disk aspect ratio is $\sim$0.07-0.09 over the disk.

The h_c obtained from the spiral model result is too low for the disk. One possible

doi:10.6342/NTU201900272

reason is that the spiral model is only suitable for linear and weakly non-linear regions. However, with the uncertainties of the parameters obtained from the best-fit, the h_c of 0.03 is within the expected disk aspect ratio of ∼0.07.

I also find second-best fit results with higher limit bounded h_c to the arm 1 and arm 2 fittings. These results have smaller adjust r-square than low h_c cases. The h_c and the predicted planet location (r_c, θ_0) are not independent. As the upper bound value of h_s increases, these fitting have favored in the largest h_c, up to the bounds. The higher the h_c is, r_c would be smaller and closer to the phase center(the stellar location). However, larger h_c would produce too much infrared flux for the SED fitting (Andrews et al., 2011). The h_c in upper limit bounded cases is not well constrained.

With the physical value range of disk aspect ratio ($0.03 < h_c < 0.2$ (Andrews et al., 2011)), upper limit bounded is also a possible result. The disk aspect ratio obtained from the spiral model to the spirals seen in the NIR polarized image is 0.18 (Grady et al., 2013) and 0.2 (Benisty et al., 2015). The planet locations of our arm 1 and arm 2 suggested by the upper limit of h_c are similar to the one determined by Benisty et al. (2015) with the same disk aspect ratio.

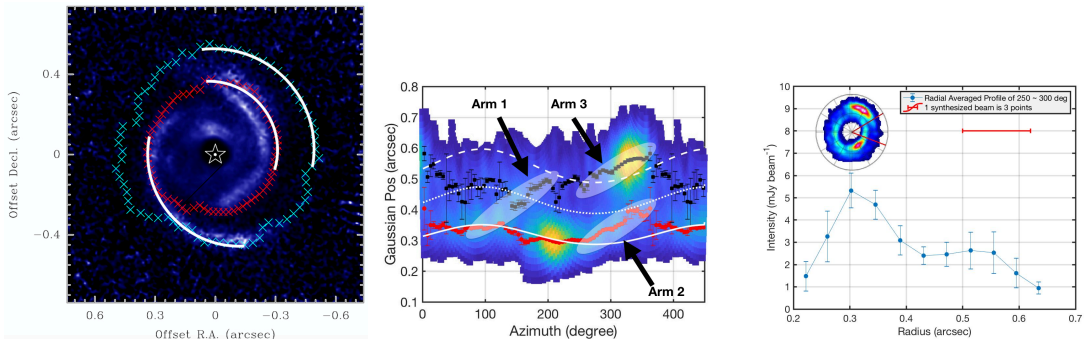

Figure 4.1: (a): Polarized intensity image (color scale) with peak locations (marked as red and cyan crosses) from the two Gaussian fitting. Both the NIR image and peak locations are projected. (b): Triple rings (marked as white solid, dotted and dashed curves) identified by Dong et al. (2018) superimposed with the deprojected image and the peak locations (marked as red dots and black squares) in the radius and azimuth coordinates. The SE spiral at ∼ 250° clearly deviates from the elliptical inner ring identified by Dong et al. (2018). (c): Analysis method by Dong et al. (2018) applied to our ALMA image. The blue dots are the intensities averaged in azimuth ranging from 250° to 300° every 0.″04 in radius. A wider inner ring at ∼0.″35 is seen, which we identify as the arm 2 spiral using our two Gaussian analyses.

doi:10.6342/NTU201900272

4.2 Comparison with NIR

Fig 2.1c shows the NIR emission in color scale and sub-mm emission in contour. It shows different geometry in different wavelengths. Fig 4.1a overlays the peak locations obtained from our analysis with the NIR image in order to compare the spatial locations of structures traced with these two wavelengths. The arm 3 in sub-mm has no counterpart in the NIR image. Instead, there is a clear spatial offset of 0.″2 in sub-mm from the emission in the NIR image at the same position angle (Marino et al., 2015). The southwest arc is located at a larger radius than the NIR image. The southeast sub-mm emission is seen in part of match and part of the outer rim of the spiral seen at the NIR image with cyan crosses from 140° to 205° on Fig 4.1a. The differences show that they are tracing different material. We'll have further discussion in next paragraph.

4.3 Scenario of sub-mm and NIR observations

We present a possible scenario to explain the difference between our sub-mm observation and the previous NIR polarized emission. The difference comes from the disk geometry. With the trailing sense of the NIR spirals and the major axis at 65°, northwest side is the near side. With the sense of the NIR emission is scattered on the sub-mm dust grain and thus located at the inner edge, differences at arm 2 can be explained. For the additional arc in the NIR emission at northwest, which is also located at the inner part of arm 3. It may also be the scattered emission by the tail of southwest arc but at the bottom side of the disk. Southeast, the far side, the NIR emission is also at the inner edge but with a smaller shift. With the far side sense, the spatial difference between two difference wavelengths should be smaller. Overall, the difference can be explained by scatter and the disk geometry of near far side.

doi:10.6342/NTU201900272

4.4 A spiral or an additional ring

We use our analysis method (Sec. 3.1) and identify three spirals (Sec 3.2). However, at west, Dong et al. (2018) resolved triple elliptical rings with a higher resolution (0.″04) ALMA image. In their scenario, the region where we identify the spiral is an ellipsoidal inner ring and the middle ring. The middle ring is located at the end of our arm 2 at ∼0.″4 in radius and ∼300° in azimuth. However, instead of rings, we identify a spiral which the peaks continuously move outward from 250° to 365 ° in azimuth with a 0.″1 shift in radius. Here we discuss the possible results of whether it is a spiral or an additional ring.

4.4.1 The middle ring

Dong et al. (2018) analyzed the disk structure by averaging the ring regions in azimuthal direction to get the radial profiles. In the averaged radial profile of west ring region, they identified three bumps at ∼0.″29, ∼0.″4 and ∼0.″51 in radius as the triple rings. The middle ring have an intensity of 0.32 mJy beam^{-1}. The local minimum between the inner and the middle ring is 0.28 mJy beam^{-1} at ∼0.″36 in radius. The full width (from the peak to the minimum) of the inner ring is 0.″06, which is as much as the radial shift of our arm 2 in the same region.

4.4.2 A spiral

Instead of rings, we identify a spiral structure at west with our lower resolution data and our analysis method. Instead of averaging in azimuthal direction to get the radial profile, I split the disk into segments by azimuth. In each segment, I fit two Gaussian functions to the radial profile to represent the peak locations. Based on my analysis, we see a continued change in radius of the peak locations through azimuthal direction.

It is striking that the two spirals identified using our analysis have similar patterns. Fig 4.2 shows the result. The black boxes at the upper panels are the two spiral regions we identified in Sec 3.2. They are 160° separated in azimuth. We shift and overlay the black boxes to check the patterns of our spirals. In the intensity panel (Fig 4.2c), both of the two

doi:10.6342/NTU201900272

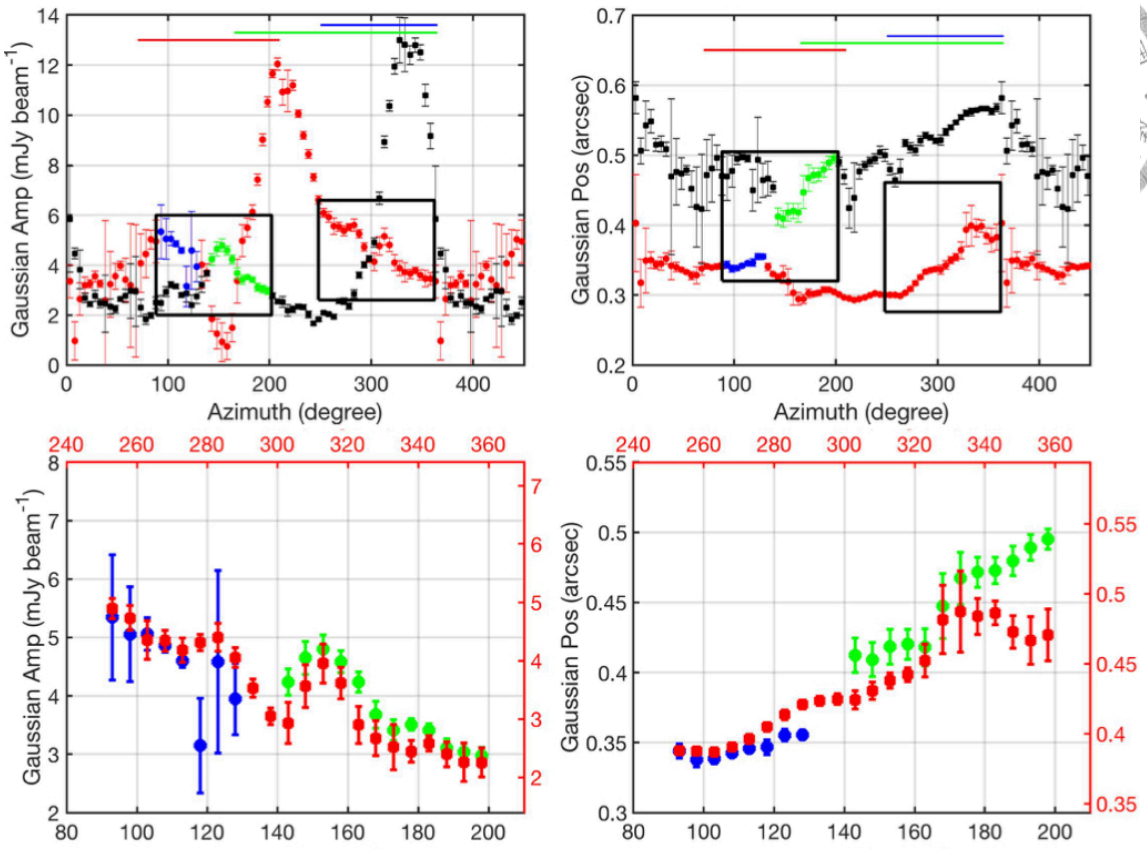

Figure 4.2: Shift and overlay of the two spiral regions, which shows the similar patterns of the spiral features. Upper panels are Fig 3.2d, e superimposed with two boxes at the two spiral regions. SE spiral (arm 1) is located from 90° to 200° in azimuth. Arm 2 is located from 250° to 360° in azimuth. Blue circles are the SE spiral identified by the inner Gaussian. Green squares are the SE spiral identified by the outer Gaussian. Connecting the blue circles and the green squares is the arm 1. Lower panels are the results of shifting 160° in azimuth to the two spiral regions. Shifts in the amplitude and position are 0.6 mJy beam^{-1} and 0.″04, respectively. Black and red axes are for the arm 1 and 2, respectively. It shows similar patterns of the two spirals.

spiral features have a gradually decrease but a small bump in the intensity. In the position panel (Fig 4.2d), the two spiral features are moving outward with a little difference in the pitch angle. The patterns of my two spirals show similarity in the intensity and position panels.

I superimposed the triple elliptical rings proposed by Dong et al. (2018) on my data in Fig 4.1b. (See appendix L for how I plot the elliptical rings). We compare the difference between the peak locations (red circles) and the elliptical inner ring (white solid line) at west (∼300°). The arm 2 at ∼ 250° clearly deviates from the elliptical inner ring. Our arm 2 is extended to the inner part of the north clump and reach their middle ring. The spiral

doi:10.6342/NTU201900272

we identified is not consisted of elliptical rings.

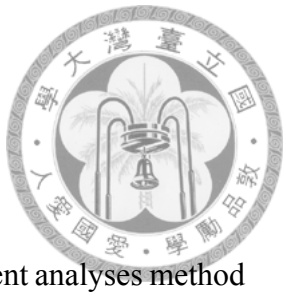

4.4.3 What is the difference

Comparing my results with Dong et al. (2018), we are using different analyses method to different data. They used their method to their data and claimed triple rings, while I use my method to my data and identified spirals. In order to compare with their result, I follow their method to analyze my data. I select the data between 250° and 300° in azimuth as the ring west. The region is selected within 15 sigma level (6 mJy beam^{-1}) to avoid the two clumps. Fig 4.1c shows the result. We identify a wider inner ring using their method, while the information of a spiral is hidden inside. We can also identify a more azimuthal extended spiral using my method.

Their method is picking up the information radially because they averaged in a region of azimuth. My method is getting the information in azimuthal direction as I split the disk into segments then analyze. I read the radial profile in each segment by fitting two Gaussian components. In addition, my method can analyze the structures in the clump regions, where my spiral is extended to. We don't detect three components in one segment simultaneously with our lower-resolution image. The methods to analyze the disk structure are the main difference between us.

To further compare, we plot our results on their image in Fig 4.3. Red dots and black squares are my peak locations. Three white transparent masks are the three arms we identified. The deprojected images are from Dong et al. (2018) with different color map for different panels. In right panels, we use a four-color only color map to enhance the contrast of the image. We mask our three arms and try to figure out the counterparts in higher-resolution ALMA image. In Fig 4.3b, it is shown that the arms we identified is also detected in the image from Dong et al. (2018).

doi:10.6342/NTU201900272

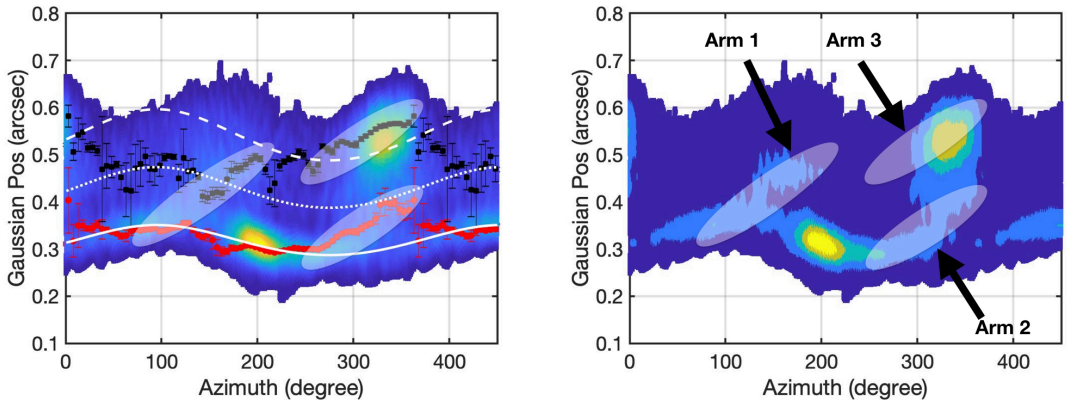

Figure 4.3: In all panels, three transparent masks are the three arms we identified. (a): Our peak locations (red dots and black squares) superimposed with the deprojected image and triple elliptical rings (marked as white solid, dotted and dashed lines) identified by Dong et al. (2018). (b): Deprojected image from with a four-color only color map to enhance the contrast. The arms we identified is also detected in the higher-resolution ALMA image.

doi:10.6342/NTU201900272

Chapter 5

Summary

We reproduce the image from ALMA band 7 archival data with robust and superuniform weighting. The resolutions are 0.″18 and 0.″12 and the noise level are 92 μJy beam^{-1} and 0.4 mJy beam^{-1} for the robust and SU weighting, respectively. The continuum emissions show asymmetrical structures.

We split the disk into segments and fit Gaussians to the radial profile. We fit an ellipse to the inclined peak locations. The ellipse is not from a projection effect of a circular ring. The ellipse center does not match with the phase center.

We do the same analysis to the SU weighting image. We analyze the best-fit parameters as a function of azimuth. We identified three structures by the local minimums in intensities. The first structure is the north clump at a larger radius (arm 3). The peak locations move inward clockwise from 0.″58 to 0.″46 from 365° to 250° with the pitch angle of $\sim$7.4°. The second structure (arm 2) is the south clump with a tail like structure. The peak locations move outward form 0.″29 to 0.″4 from 250° to 365° with the pitch angle of $\sim$9.4°. The third structure is the southeast spirals (arm 1). We connect the inner Gaussian and the outer Gaussian in this feature by following the brighter emission. The peak locations move outward from 0.″34 to 0.″49 from 70° to 210° with the pitch angle of $\sim$10.2°.

We calculate the Toomre Q parameter of the disk. The disk is gravitationally stable. We calculate the line dispersion at the continuum emission peaks and compare with thermal contribution. There is no clear turbulence level. We compare our results with the NIR spirals and higher-resolution image (Benisty et al., 2015; Dong et al., 2018).

doi:10.6342/NTU201900272

Chapter 6

Conclusion

In order to analyze the asymmetric features, which provide indirect evidences of planet formation, we obtain and analyze the continuum emission of the circumstellar disk around MWC 758. We identify the peak locations by fitting two Gaussian functions to the intensity profile of each segment (every 5° in azimuth). Based on the variation of the peak locations as a function of azimuth, we identify three spirals. The spirals can be explained by the pattern of density waves induced by planets. Three planets for three spiral patterns. The disk aspect ratio (0.2) and two planet locations are similar to the previous NIR result (Benisty et al., 2015).

We compare our spirals with NIR spirals, which appear at smaller radius of our mm observation. The spatial offset between the two wavelengths are larger at the southeast and smaller at the northwest. The differences can be well explained by the scattering on the inner edge and projection effect between the near and far side.

We compare our results with a higher-resolution ALMA image. Dong et al. (2018) presents triple rings in the west, while we identified a spiral. The difference comes form the resolution of the images and the method of analysis.

doi:10.6342/NTU201900272

Appendix A

Intensity profile of segments (robust)

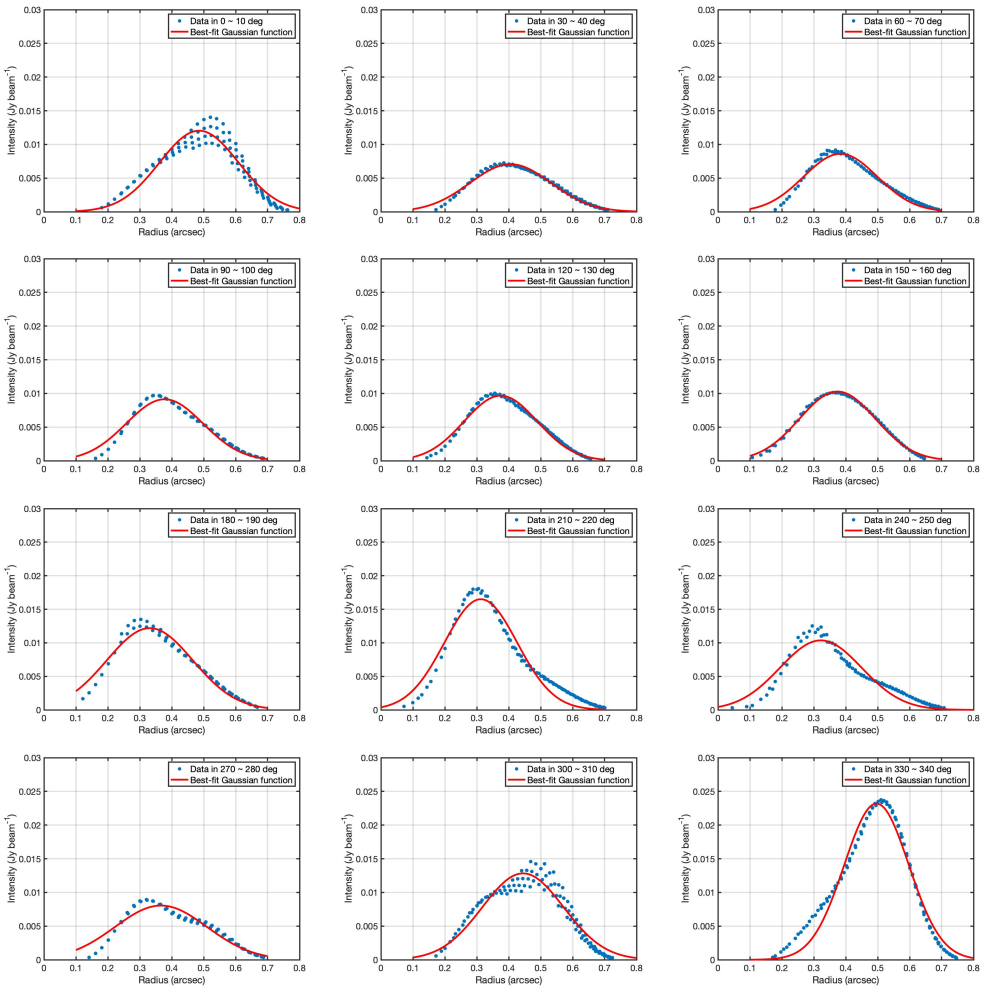

Figure A.1: Plots of the inclined continuum intensity profile (robust) at 5°, 35° , ... , 335°. The axes are distance to the central star in arcsec and intensity in Jy beam^{-1}. Blue dots are the data points inside a segment. Red curves are the best-fit Gaussian function.

doi:10.6342/NTU201900272

Appendix B

Intensity profile of segments (SU)

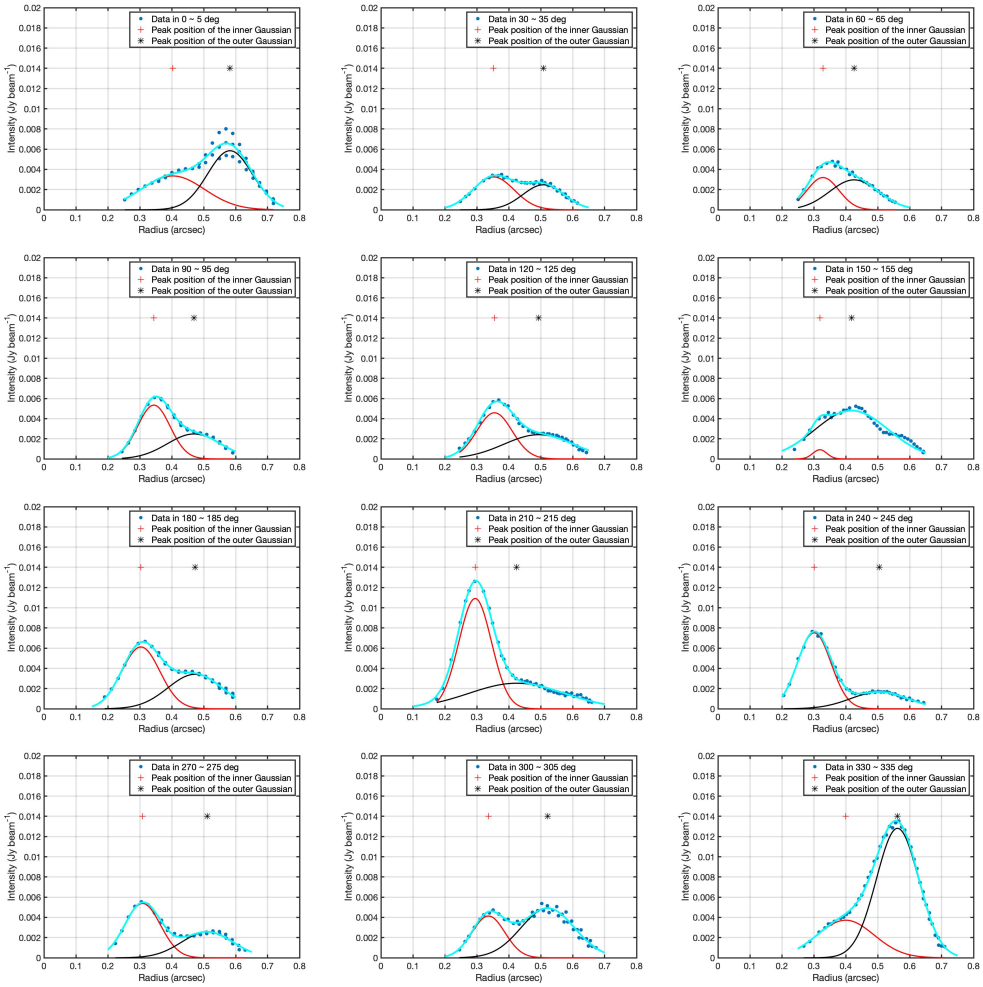

Figure B.1: Plots of the deprojected continuum intensity profile (SU) at 3°, 33° , ... , 333°. The axes are distance to the central star in arcsec and intensity in Jy beam^{-1}. Blue dots are the data points inside a segment. Cyan curves are the best-fit two Gaussian functions. Red and black curves are the inner and outer Gaussians, respectively. Red plus and black asterisk are the peak position of the two Gaussians.

doi:10.6342/NTU201900272

Appendix C

Intensity profile at 270°-330° (SU)

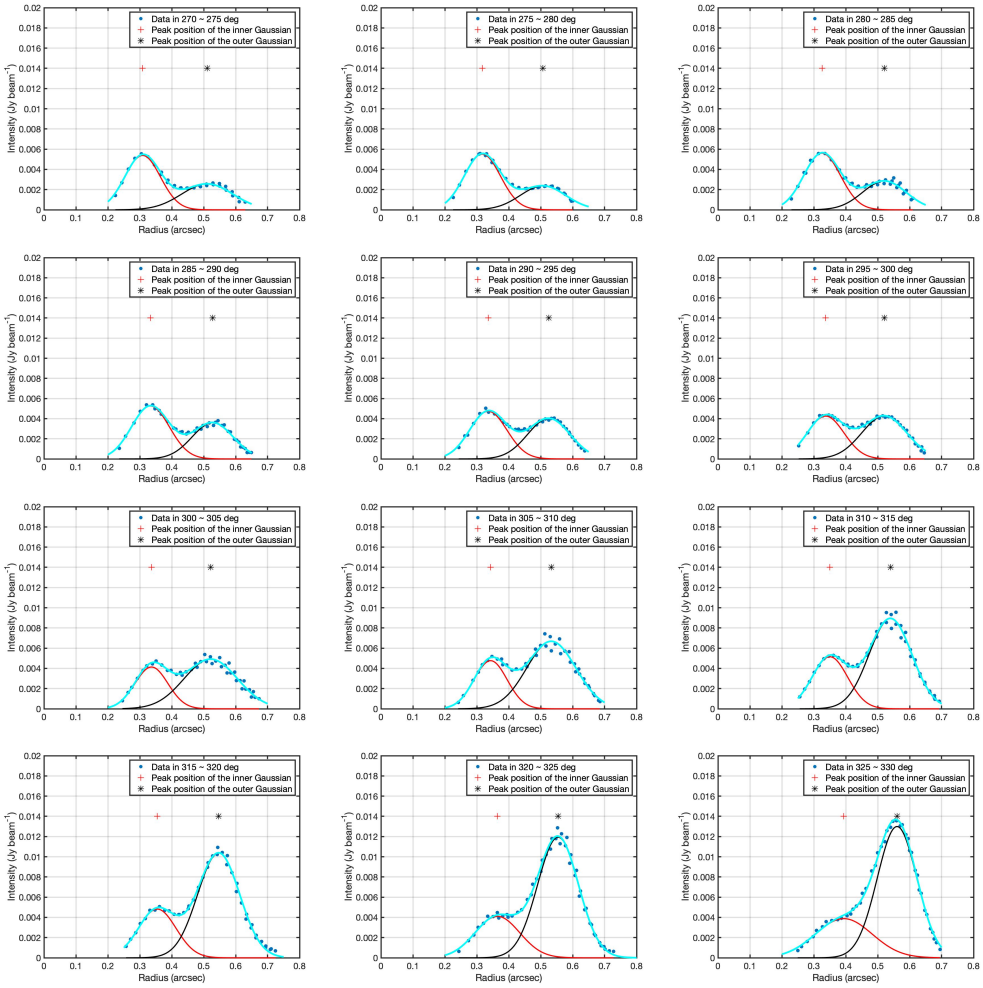

Figure C.1: Plots of the deprojected continuum intensity profile (SU) at 273°, 278° , ... , 328°. The axes are distance to the central star in arcsec and intensity in Jy beam^{-1}. Blue dots are the data points inside a segment. Cyan curves are the best-fit two Gaussian functions. Red and black curves are the inner and outer Gaussians, respectively. Red plus and black asterisk are the peak position of the two Gaussians.

doi:10.6342/NTU201900272

Appendix D

ALMA

ALMA is the abbreviation of Atacama Large (sub)Millimeter Array. It is one of the best interferometer in the world. Taiwan is also part of the partnership. The array is located in Atacama Desert of Chile on the 5,000 m elevation. ALMA has 66 telescope in total with 54 in 12 meter and 12 in 7 meter.

Figure D.1: Picture of nineteen ALMA antennas on the Chajnantor plateau. Credit: ALMA (ESO/NAOJ/NRAO)

doi:10.6342/NTU201900272

Appendix E

Distance from Gaia DR2

In order to get the distance of MWC 758, we used the latest result from Gaia Data Release 2. The parallax is the displacement of an object observed at two different position. The parallax of MWC 758 is 6.629203027121364 $\pm$ 0.3840402204775034 mas. The distance of the object is one over the parallax.

$$Distance = (\frac{1}{Parallax}) \tag{E.1}$$

Calculated with the errors, the distance of MWC 758 is $150.848151^{+9.27}_{-8.26}$ parsec.

doi:10.6342/NTU201900272

Appendix F

Fitting an Ellipse

The method to direct least square fitting of ellipses was carried out by Fitzgibbon et al. (1996). It's a ellipse-specific and non-iterative method for fitting ellipses. Halir & Flusser (1998) improved the algorithm with practical and numerically stable solutions.

doi:10.6342/NTU201900272

Appendix G

Monte Carlo Method for error bars of Ellipsoidal Fit

With the ability to fit an ellipse, we want to determine the error bars of the parameters. We use the Monte Carlo method for the purpose. The Monte Carlo method is to repeat the procedures, which has adjustment with random sampling, as many times as possible, then discuss the distribution of the outcomes. We shift every peak locations with a normal distribution of their error bars, which was the 95% confident level get by the Gaussian fittings. We fit an ellipse to the shifted peak locations and get one set of the parameters of the ellipse. We repeated the above procedures a hundred thousands times. We do the statistic analysis to the ellipse parameters (The center shifts, P.A., Inclination) and get the results with error bars.

doi:10.6342/NTU201900272

Appendix H

Gaussian-Hermite function

$$I(r) = A\ exp(-\frac{(x-\mu)^2}{2\sigma^2})\ \left\{1 + h_3(c_1 y + c_3 y^3) + h_4(c_0 + c_2 y^2 + c_4 y^4))\right\} \qquad \text{(H.1)}$$

The Gaussian-Hermite (GH) function is a superposition of Gaussian function and Hermite polynomial. Hermite polynomial is a complete and orthogonal system. With two additional terms, we can trace the asymmetrical structure of the Gaussian function. Although, we can get the second peak (if exists) of the GH function with some calculation. The main problem is that, if there are two peaks with similar intensities in one profile, it is not well-fitted by the GH function because it is based on a single Gaussian function. Using two Gaussian functions to fit the profiles is direct and consistent with the results obtained by GH, so we choose two Gaussian functions to fit the deprojected SU profiles.

doi:10.6342/NTU201900272

Appendix I

Pitch angle

Pitch angle is the angle between the tangential and azimuthal direction of the point. The azimuthal length can be calculated by the circumference of the segments. The radial shift, which is the evidence of a spiral, was obtained from our two Gaussian fittings. The definition of the pitch angle is,

$$Pitch\ angle = arctan(\frac{Azimuthal\ length}{Radial\ shift}) \tag{I.1}$$

doi:10.6342/NTU201900272

Appendix J

Sound speed in disks

$$c_s = \sqrt{\frac{\gamma kT}{\mu m_H}} \tag{J.1}$$

c_s is the sound speed. γ is the adiabatic index, which equals to one if it is an ideal gas and isothermal. k is the Boltzmann constant. T is the disk temperature from Boehler et al. (2018). μ is 2.8, the mean molecular weight. m_H is the hydrogen mass. With the careful calculation in the unit, the sound speed in the disk is $\sim$0.5km.

doi:10.6342/NTU201900272

Appendix K

Molecular lines

To compare the turbulence level with the thermal contribution, we calculated the line dispersion at the peaks for the turbulence level. The optical depth of the dust is $\sim$1, which is not negligible, so we use the no continuum subtraction line data. ^{13}CO is a thicker line than C^{18}O. So we use ^{13}CO with no continuum subtraction (ncs) as the tracer for the velocity dispersion. We fit one Gaussian function to the velocity profiles at the north and south peaks and then calculate the velocity dispersion.

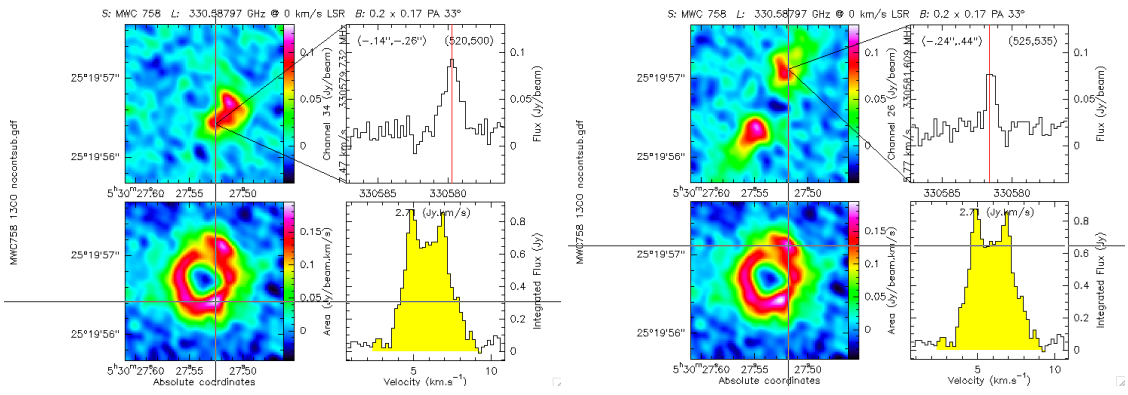

Figure K.1: Line width analysis to south (left panel) and north (right panel) peaks of ^{13}CO line emission without continuum subtraction. Compare the Gaussian width and the sound speed (Sec. 3.5), there is no clear turbulence level.

doi:10.6342/NTU201900272

Appendix L

Plotting the ellipsoidal ring in Dong et al. (2018)

Instead of the center of the ellipses, the phase center of the MWC 758 is locating at the focus of the triple elliptical rings. To plot the final ellipse, we first plot an ordinary, centered and no-orientation ellipse with the semi major axis (a=0″.319±0.02) and the eccentricity (e=0.1±0.01). Second, we rotate the ellipse 5° in azimuth to set the major axis at the position angle (95°±10°) (Dong et al., 2018). Third, we shift the whole ellipse to set the center at the focus. We repeated the above procedures to get the middle ring (1.35 times larger than the inner ring) and the outer ring (1.7 times in size than the inner ring).

doi:10.6342/NTU201900272

Bibliography

Andrews, S. M. 2015, PASP, 127, 961

Andrews, S. M., Wilner, D. J., Espaillat, C., et al. 2011, ApJ, 732, 42

Benisty, M., Juhasz, A., Boccaletti, A., et al. 2015, A&A, 578, L6

Boehler, Y., Ricci, L., Weaver, E., et al. 2018, ApJ, 853, 162

Christiaens, V., Casassus, S., Perez, S., van der Plas, G., & Ménard, F. 2014, ApJL, 785, L12

Dong, R., Liu, S.-y., Eisner, J., et al. 2018, ApJ, 860, 124

Dutrey, A., Semenov, D., Chapillon, E., et al. 2014, Protostars and Planets VI, 317

Fitzgibbon, A. W., Pilu, M., & Fisher, R. B. 1996, in Proceedings of 13th International Conference on Pattern Recognition, Vol. 1, 253–257 vol.1

Grady, C. A., Muto, T., Hashimoto, J., et al. 2013, ApJ, 762, 48

Halir, R., & Flusser, J. 1998, Numerically Stable Direct Least Squares Fitting Of Ellipses, ,

Holl, B., Audard, M., Nienartowicz, K., et al. 2018, A&A, 618, A30

Isella, A., Natta, A., Wilner, D., Carpenter, J. M., & Testi, L. 2010, ApJ, 725, 1735

Kanagawa, K. D., Muto, T., Tanaka, H., et al. 2015, ApJL, 806, L15

Kraus, S., Kreplin, A., Fukugawa, M., et al. 2017, ApJL, 848, L11

doi:10.6342/NTU201900272

Lin, C. C., & Shu, F. H. 1964, ApJ, 140, 646

Long, F., Pinilla, P., Herczeg, G. J., et al. 2018, ArXiv e-prints, arXiv:1810.06044

Marino, S., Casassus, S., Perez, S., et al. 2015, ApJ, 813, 76

Meeus, G., Montesinos, B., Mendigutía, I., et al. 2012, A&A, 544, A78

Muto, T., Grady, C. A., Hashimoto, J., et al. 2012, ApJL, 748, L22

Muto, T., Tsukagoshi, T., Momose, M., et al. 2015, PASJ, 67, 122

Ogilvie, G. I., & Lubow, S. H. 2002, MNRAS, 330, 950

Ossenkopf, V., & Henning, T. 1994, A&A, 291, 943

Rafikov, R. R. 2002, ApJ, 569, 997

Reggiani, M., Christiaens, V., Absil, O., et al. 2018, A&A, 611, A74

Thi, W. F., van Dishoeck, E. F., Blake, G. A., et al. 2001, ApJ, 561, 1074

van der Marel, N., Cazzoletti, P., Pinilla, P., & Garufi, A. 2016, ApJ, 832, 178

Zhu, Z., & Stone, J. M. 2014, ApJ, 795, 53

doi:10.6342/NTU201900272